



**UNIVERSIDADE ESTADUAL DE CAMPINAS  
SISTEMA DE BIBLIOTECAS DA UNICAMP  
REPOSITÓRIO DA PRODUÇÃO CIENTÍFICA E INTELECTUAL DA UNICAMP**

**Versão do arquivo anexado / Version of attached file:**

Versão do Editor / Published Version

**Mais informações no site da editora / Further information on publisher's website:**

<https://iopscience.iop.org/article/10.1088/1361-6463/aaccc3>

**DOI: 10.1088/1361-6463/aaccc3**

**Direitos autorais / Publisher's copyright statement:**

©2018 by Institute of Physics Publishing. All rights reserved.

DIRETORIA DE TRATAMENTO DA INFORMAÇÃO

Cidade Universitária Zeferino Vaz Barão Geraldo

CEP 13083-970 – Campinas SP

Fone: (19) 3521-6493

<http://www.repositorio.unicamp.br>

# Strategies to tailor the architecture of dual Ag/Fe-oxide nano-heterocrystals—interfacial and morphology effects on the magnetic behavior

P Tancredi<sup>1</sup>, O Moscoso Londoño<sup>2,3,6</sup> , P C Rivas Rojas<sup>1</sup>, U Wolff<sup>4</sup>,  
L M Socolovsky<sup>5</sup>, M Knobel<sup>2</sup> and D Muraca<sup>2</sup>

<sup>1</sup> Facultad de Ingeniería, Laboratorio de Sólidos Amorfos, Instituto de Tecnologías y Ciencias de la Ingeniería ‘Hilario Fernández Long’, Universidad de Buenos Aires—CONICET, Buenos Aires, Argentina

<sup>2</sup> Instituto de Física ‘Gleb Wataghin’, Universidade Estadual de Campinas, Campinas, Brazil

<sup>3</sup> Facultad de Ingeniería, Universidad Autónoma de Manizales, Antigua Estación del Ferrocarril, Manizales, Colombia

<sup>4</sup> IFW Dresden, Leibniz Institute for Solid State and Materials Research, Dresden, Helmholtzstrasse 20, 01069 Dresden, Germany

<sup>5</sup> Facultad Regional Santa Cruz, Universidad Tecnológica Nacional - CIT Santa Cruz (CONICET), Río Gallegos, Argentina

E-mail: [omoscoso@ifi.unicamp.br](mailto:omoscoso@ifi.unicamp.br) and [oscar.moscosol@autonoma.edu.co](mailto:oscar.moscosol@autonoma.edu.co)

Received 2 April 2018, revised 10 June 2018

Accepted for publication 14 June 2018

Published 29 June 2018




## Abstract

Bifunctional nanostructured architectures have shown appealing properties, since a single entity can combine the diverse properties of its individual constituents. Particularly, by growing Fe-oxide domains over Ag nanoparticles, the plasmonic and superparamagnetic properties can be combined in a single particle. Beyond the multifunctionality of this system, there are several properties that emerge from intrinsic factors, such as: interface and/or morphology. In this study, we present the synthesis protocols to obtain two sets of heterocrystals, each one with different morphology: dimer and flower-like. In addition, the magnetization behavior of these hybrid nano-heterocrystals is investigated and discussed. These nanomaterials were built by a seed assisted heterogeneous nucleation process, carried out in organic solvents of high boiling point, using the same batch of silver nanoparticles with a mean size of 6 nm as seeds, and tuning the electron-donor capacity of the reaction environment at the thermal decomposition of the iron precursor. Ag/Fe<sub>3</sub>O<sub>4</sub> heterocrystals with dimer and flower-like morphologies were obtained. The synthesis protocols for generating these types of nanomaterials are discussed step-by-step. Structural and morphological properties were determined by transmission electron microscopy, x-ray diffraction and x-ray absorption fine structure. DC magnetization results suggest that the silver/magnetite coupling generates an increase of the blocking temperature in comparison to those obtained from pure magnetite. This behavior could be linked to a possible increase in the magnetic anisotropy produced by an additional disorder at the Ag–Fe<sub>3</sub>O<sub>4</sub> interface. The higher interface area of the Ag/Fe<sub>3</sub>O<sub>4</sub> heterocrystals with flower-like architecture leads to a higher blocking temperature and a stronger magnetic anisotropy. These results are supported by AC susceptibility data.

<sup>6</sup> Author to whom any correspondence should be addressed.

Keywords: hybrid nanostructures, interface effects, magnetic-plasmonic properties, superparamagnetism

 Supplementary material for this article is available [online](#)

(Some figures may appear in colour only in the online journal)

## Introduction

In the last few years, a prominent part of the research in nanochemistry has focused on the preparation of multifunctional and heterostructured nanocrystals, capable of combining two or more inorganic materials into a single system through a direct atomic bond at the interface and without the presence of a molecular bridge [1–3]. In these new heterocrystals, the properties of the different components can be combined or can give rise to new features associated to morphology or interface effects, factors that may partially govern the physicochemical behavior of these new kind of systems.

Nanoparticles that combine a noble metal (Au, Ag) with ferrite type oxides ( $\text{Fe}_3\text{O}_4$ ,  $\text{CoFe}_2\text{O}_4$ ,  $\text{Co}_3\text{O}_4$ ,  $\text{MnFe}_2\text{O}_4$ ) are among the systems that have gained major interest. In these peculiar nanostructures, the optical properties of metallic nanoparticles and the magnetic properties of Fe-oxide counterparts can be coupled. This dual behavior opens the door to new applications in several fields, including catalysis [4, 5], antimicrobial agents [6, 7], magnetic and photo/magnetic hyperthermia therapies [8, 9] and surface-enhanced Raman scattering substrates (SERS) [10], among others.

The most common process to produce heterostructured nanocrystals is the so-called seed-assisted method, where a second component is heterogeneously nucleated over previously formed nanoparticles ('seeds') of a first component. In this process, the heterogeneous nucleation of the second material is favored over homogeneous nucleation, especially when there is some compatibility between the cell parameters of the crystals [10]. Depending on the nucleation events and the growth evolution, the formed heterostructures can show distinct architectures, such as core-shell, dimer or flower-like. Many efforts have been dedicated to the understanding of the synthesis conditions and mechanisms that lead to these different morphologies [2, 11–13], mainly because the macroscopic properties of the system can be controlled or tuned by the interface type and the interactions between the different constituents.

In this work, we study the synthesis and the magnetic response of two Ag/ $\text{Fe}_3\text{O}_4$  heterostructures with different morphologies: dimer and flower-like type, prepared by a seed-assisted route in organic solvents of high boiling point. In particular, we investigate how the solvent nature, associated to its electron-donor capacity, determines the final morphology. Correspondingly, we performed a complete magnetic characterization by means of DC and AC magnetization techniques to understand how the heterostructures architecture and the distribution of the  $\text{Fe}_3\text{O}_4$  domains define the macroscopic

behavior of the samples. A discussion on the structural and optical properties is also presented to reinforce the results and the conclusions.

## Experimental details

### Materials

Silver nitrate ( $\text{AgNO}_3$ ,  $\geq 99\%$ , Sigma-Aldrich), sodium acetate ( $\text{NaCH}_3\text{COO}$ ,  $\geq 99\%$ , Anedra), oleylamine ( $\text{C}_{17}\text{H}_{31}\text{CH}_2\text{NH}_2$ ,  $\geq 99\%$ , Sigma-Aldrich), oleic acid ( $\text{C}_{17}\text{H}_{31}\text{COOH}$ , 90%, Sigma-Aldrich), 1-octadecene ( $\text{C}_{18}\text{H}_{36}$ , 90%, Sigma-Aldrich), diphenyl ether ( $(\text{C}_6\text{H}_5)_2\text{O}$ , 98%, Sigma-Aldrich), iron(III) acetylacetonate ( $\text{Fe}(\text{acac})_3$ , 99%, Sigma-Aldrich) and 1,2-hexadecanediol ( $\text{C}_{16}\text{H}_{34}\text{O}_2$ , 90%, Sigma-Aldrich). All chemicals were used as received without further purification.

### Methods

Ag/ $\text{Fe}_3\text{O}_4$  nanoparticles were synthesized by a seed assisted heterogeneous nucleation process in organic solvents of high boiling point, as described below.

### Silver Seeds Nanoparticles (AgNPs) synthesis

AgNPs were prepared according to previous reports [8, 12]. Briefly, 2 mmol silver acetate ( $\text{AgCH}_3\text{COO}$ ) were obtained by stoichiometric precipitation of  $\text{AgNO}_3$  and  $\text{NaCH}_3\text{COO}$ . The so-obtained white powder was dissolved in 2 mmol oleic acid, 2 mmol oleylamine and 5 ml 1-octadecene. The mixture was heated up to 175 °C under continuous stirring for 30 min to allow AgNPs formation. Finally, the system was cooled down to room temperature and the AgNPs were precipitated by the addition of ethanol and isolated by centrifugation at 3000 RPM for 15 min. The isolated solid was washed three times before being redispersed in hexane.

### Ag/ $\text{Fe}_3\text{O}_4$ heteroparticles formation

AgNPs were used as fixed seeds for  $\text{Fe}_3\text{O}_4$  heterogeneous nucleation. 1 mmol Ag (as AgNPs), 0.3 mmol  $\text{Fe}(\text{acac})_3$ , 1.5 mmol 1,2-hexadecanediol, 0.75 mmol oleic acid, 1.5 mmol oleylamine and 5 ml solvent (1-octadecene, ODE or phenyl ether, PHE) were added. The solution was maintained at 125 °C for 1 h under continuous stirring, and then heated (heating rate = 5 °C min<sup>-1</sup>) up to 260 °C for 60 min under Ar flow to allow  $\text{Fe}_3\text{O}_4$  formation. Finally, the system was cooled down to room temperature and the nanoparticles were precipitated

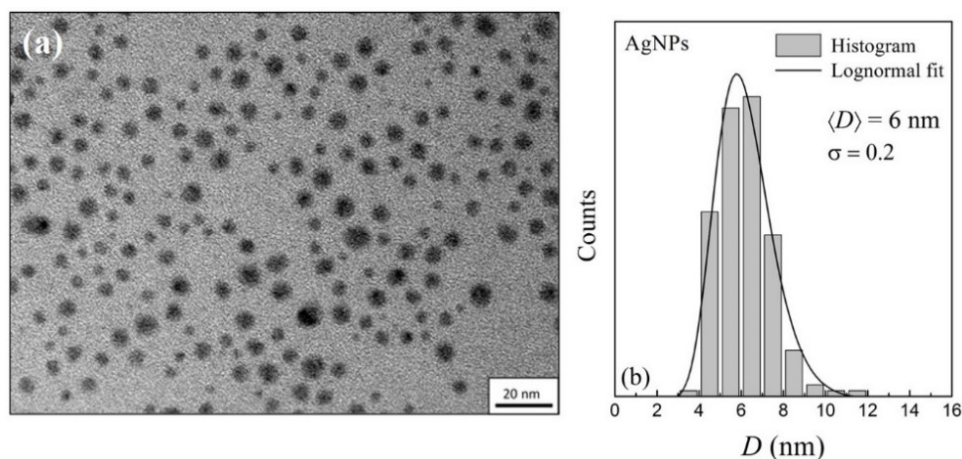


**Figure 1.** (a) TEM micrograph of AgNPs. (b) Size distribution histogram and the lognormal fit.

by the addition of ethanol and isolated by centrifugation at 3500 RPM for 30 min. The isolated solid is finally washed three times to then redisperse it in toluene.

Two samples were prepared, Ag/Fe<sub>3</sub>O<sub>4</sub> ODE (reaction carried out in 1-octadecene) and Ag/Fe<sub>3</sub>O<sub>4</sub> PHE (reaction carried out in phenyl ether). Furthermore, a control sample of homogeneously nucleated Fe<sub>3</sub>O<sub>4</sub> without the addition of the Ag seeds was prepared (see supporting information ([stacks.iop.org/JPhysD/51/295303/mmedia](http://stacks.iop.org/JPhysD/51/295303/mmedia))).

## Characterization

Phase composition and crystallographic characterization were carried out via x-ray diffraction (XRD) on a standard Rigaku diffractometer with Cu K- $\alpha$  radiation. X-ray absorption fine structure (XAFS) spectroscopy patterns for the Fe K-edge (7.112 keV) were recorded at room temperature in fluorescence mode with the colloidal samples positioned at 45° with respect to the x-ray beam. These measurements were performed at the Brazilian Synchrotron Light Laboratory (CNPEM/LNLS, Campinas, Brazil). Absorption spectra, carried out on colloidal samples (nanoparticles dispersed in toluene), were recorded at room temperature by means of a UV-vis-NIR Shimadzu UV-1603 using quartz cuvettes with 10 mm optical path length. Morphology and size distribution of the samples were determined by transmission electron microscopy (TEM) at the CNPEM/LNLS (Campinas, Brazil) in a JEOL JEM 2100F with a field emission gun (FEG) operating at 200 kV and at the IFW (Dresden, Germany) with a FEI-Tecnai microscope operating at 200 kV. The samples for TEM experiments were prepared by dripping 10  $\mu$ l of nanoparticle dispersion onto a carbon-coated copper grid (Ted Pella) and drying the solvent at room temperature. DC magnetization and AC magnetic susceptibility measurements were recorded with a MPMS-XL7 Quantum Design SQUID magnetometer and a PPMS Quantum Design magnetometer, respectively. The samples for magnetic measurements were prepared by mixing 50  $\mu$ l of the colloidal dispersion containing the Ag/Fe<sub>3</sub>O<sub>4</sub> heterocrystals and one drop of 1-octadecene. This mixture was stirred until the toluene was evaporated. After that, a piece of cotton (approx. 15 mg) was impregnated with the Ag/

Fe<sub>3</sub>O<sub>4</sub> sample and finally placed in the SQUID/PPMS holder sample.

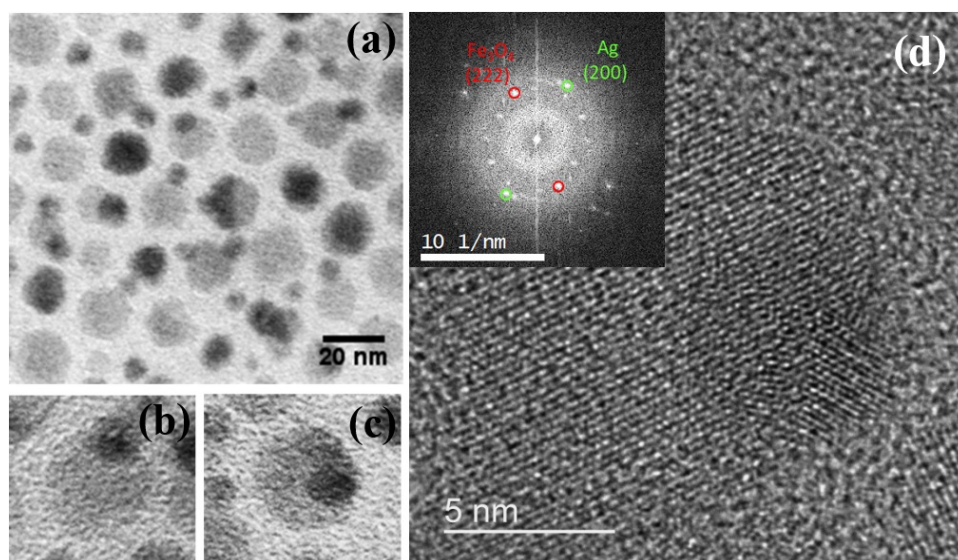
## Results and discussion

The two-step procedure employed for the Ag/Fe<sub>3</sub>O<sub>4</sub> heteroparticles synthesis can be conveniently used to study the reaction mechanism and the conditions that lead to the formation of different heterostructure morphologies.

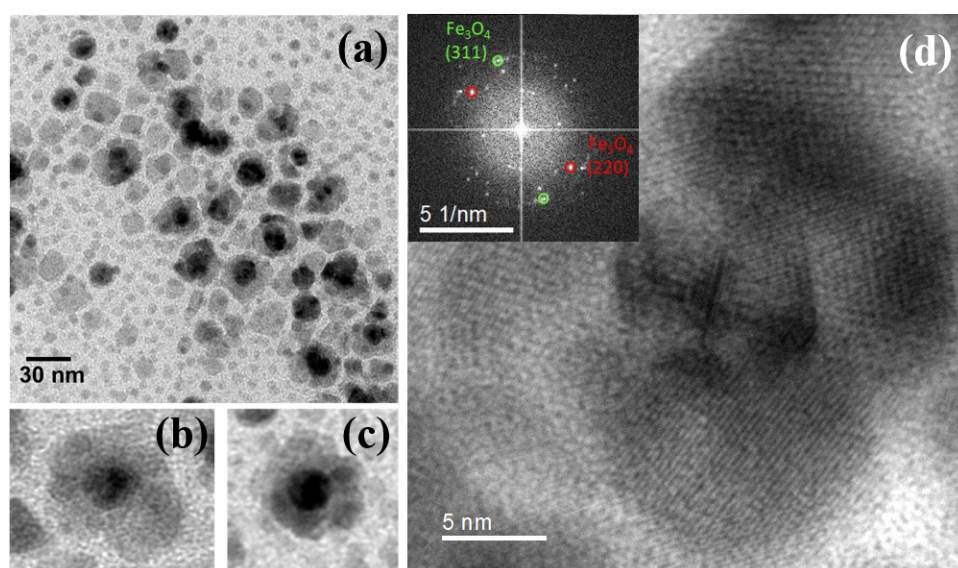
The AgNPs (produced separately in a first step) were incorporated to the synthesis medium prior to the thermal decomposition reaction and the formation of the iron oxide phase. One-step reactions have been successfully developed to produce heterocrystals by exploiting the difference between the formation temperatures of the metallic nanoparticle and the iron oxide [14–16]. In spite of this, we have decided to employ a two-step procedure so we can directly relate the heterogeneous nucleation events and final heteroparticle structure with the reaction conditions, i.e. solvent electron-donor capacity, and detach them from other variables, such as AgNPs size and concentration, for example. Reports on two-steps heterostructure synthesis have investigated different options for the iron source, including iron acetylacetonate, iron oleate or iron pentacarbonyl. However, the precursor nature does not seem to affect the final particle conformation because a common transformation to iron oleate occurs at low temperatures (prior to iron oxide nucleation) regardless the original reagent [17, 18].

Figure 1 shows a representative TEM image of the prepared AgNPs. The synthesized AgNPs show a spheroidal-like shape with a narrow size distribution. Histograms were obtained by counting more than 200 silver nanoparticles from several TEM images, which were well fitted using a lognormal function (figure 1(b)). From this, a mean diameter  $\langle D \rangle = 6 \text{ nm}$  with a rather narrow size distribution ( $\sigma = 0.2$ ) was determined. These results confirm the well-dispersed nature of the initial AgNPs colloidal suspension obtained in the first step of the synthesis. The *fcc* structure of the silver nanocrystals was examined by XRD, as is shown in figure S1 (supplementary information).





**Figure 2.** (a)–(c) Representative TEM images of Ag/Fe<sub>3</sub>O<sub>4</sub> heterostructures with dimer-like configuration showing the iron oxide nanoparticles attached to a silver seed. (d) HR-TEM image of a single dimer-like nanoparticle and corresponding Fourier transform (inset).



**Figure 3.** (a)–(c) Representative TEM images of Ag/Fe<sub>3</sub>O<sub>4</sub> heterostructures with flower-like configuration showing the iron oxide nanoparticles surrounding a silver seed. (d) HR-TEM image of a single flower-like nanoparticle. (d) HR-TEM image of a single dimer-like nanoparticle and corresponding Fourier transform (inset).

Afterwards, these AgNPs were used as fixed seeds for the formation of the Ag/Fe<sub>3</sub>O<sub>4</sub> heteroparticles in both reaction solvents. Figures 2 and 3 show the TEM and HR-TEM of the two samples. The difference in the atomic number between the two components makes it possible to distinguish iron oxide (lighter particles) from Ag (darker particles) in the images. For the heterostructures prepared in 1-octadecene (Ag/Fe<sub>3</sub>O<sub>4</sub> ODE) dimer-like heteroparticles are predominant (figure 2), with just one iron oxide crystal attached per Ag seed. On the other hand, for heterostructures prepared in phenyl ether (Ag/Fe<sub>3</sub>O<sub>4</sub> PHE) flower-like heteroparticles predominate (figure 3), with various iron oxide crystals surrounding a central Ag seed. In both TEM images (figures 2(a) and 3(a)), some non-attached iron oxide particles can be seen. However, the

presence of these particles decreased dramatically from previous samples by carefully tuning the relation between Ag seeds and Fe precursor and the heating rate. Figures 2(d) and 3(d) present the HR-TEM images for samples Ag/Fe<sub>3</sub>O<sub>4</sub> ODE and Ag/Fe<sub>3</sub>O<sub>4</sub> PHE, respectively. Additional images are displayed in the supporting information (figures S2 and S3). Notice that by applying the Fourier transformation technique on a simple dimer-like particle (inset on figure 2(d)), characteristic crystallographic planes for magnetite and silver phases can be detected, i.e. (222) plane for the Fe<sub>3</sub>O<sub>4</sub> and (200) plane for the Ag. For the sample Ag/Fe<sub>3</sub>O<sub>4</sub> PHE, the Fourier transformation (inset on figure 3(d)) reveals two characteristic crystallographic planes for magnetite phase: (220) and (311). However, none of the crystallographic planes of

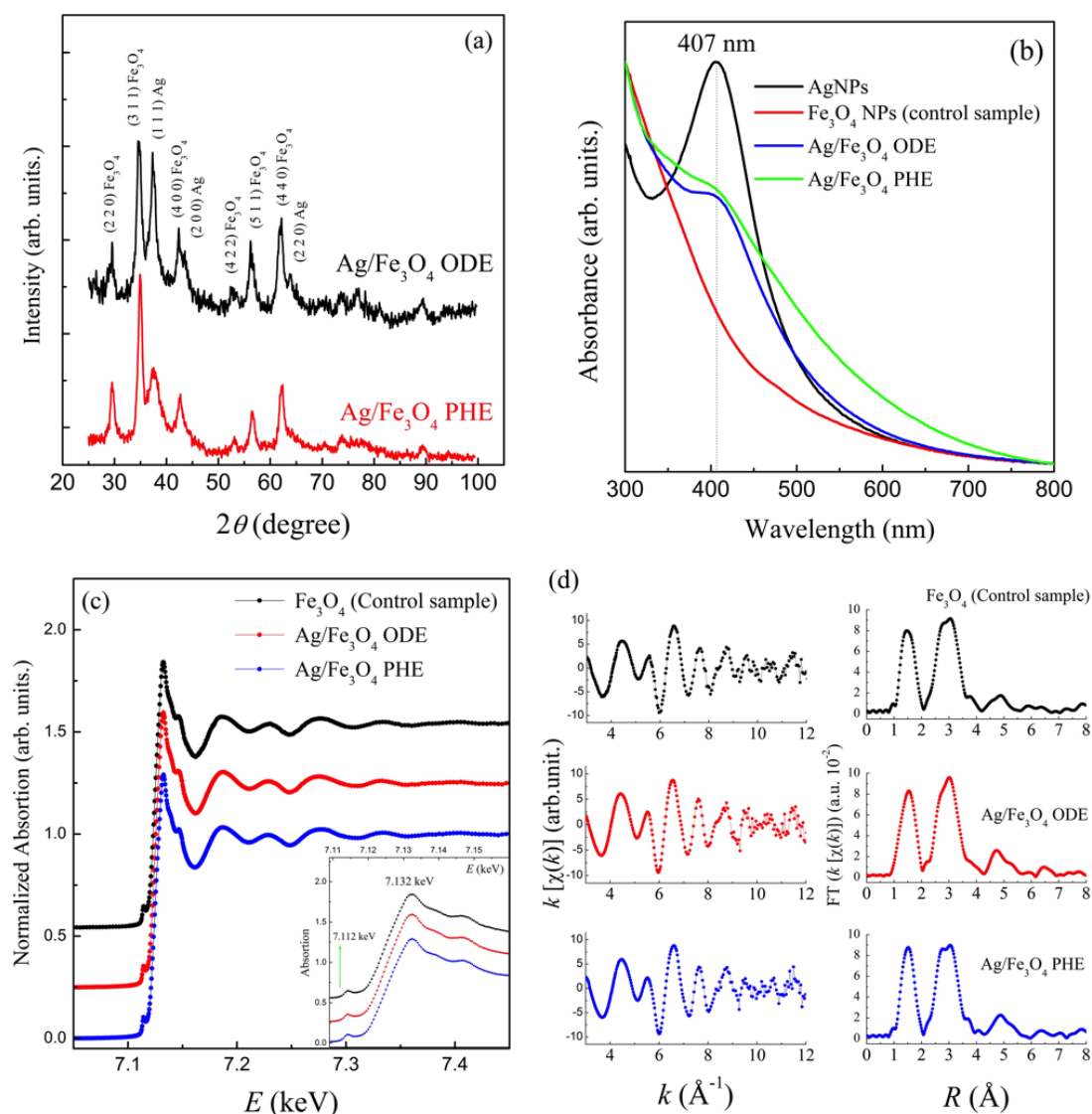


**Figure 4.** (a) XRD patterns of sample Ag/Fe<sub>3</sub>O<sub>4</sub> ODE (dimer-like morphology) and Ag/Fe<sub>3</sub>O<sub>4</sub> PHE (flower-like morphology). The phase and Miller index of principal peaks are indicated. (b) UV-vis absorption spectra of the samples. (c) Experimental EXAFS Fe K-edge spectra for samples Ag/Fe<sub>3</sub>O<sub>4</sub> ODE, Ag/Fe<sub>3</sub>O<sub>4</sub> PHE and Fe<sub>3</sub>O<sub>4</sub>. Inset: XANES region. (d) Fourier transformations obtained for the studied samples.

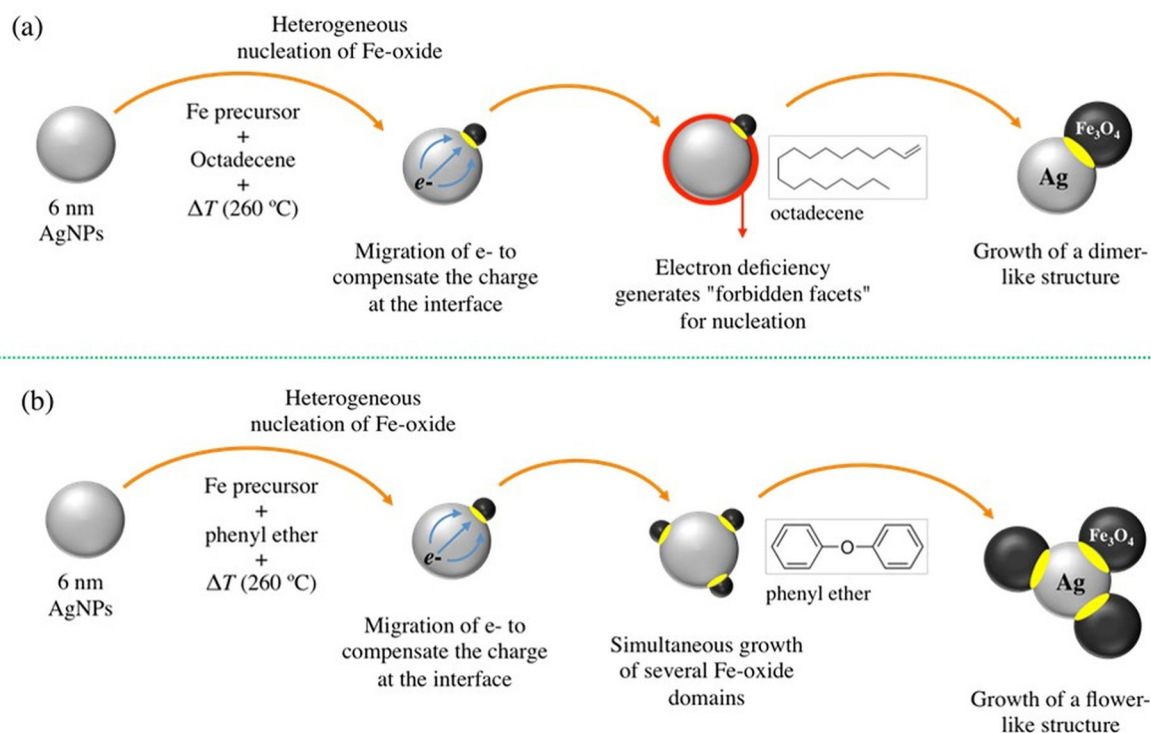
the metallic silver are distinguished, which is probably related to the absence of the oriented planes of this material in the obtained HR-TEM image.

Figure 4(a) shows the XRD patterns of the dried heterostructures. As expected, two contributions from two sets of diffraction peaks can be observed in the diffractograms. One set can be assigned to the *fcc* spinel-inverse iron oxide phase (Fe<sub>3</sub>O<sub>4</sub> and/or  $\gamma$ -Fe<sub>2</sub>O<sub>3</sub>) and the other one corresponds to *fcc* metallic Ag. Thus, one can confirm the presence of both crystalline structures in the samples.

Optical properties were studied in terms of UV-Visible absorption and the resulting spectra are shown in figure 4(b). The surface plasmon resonance peak (SRP) associated to the Ag seeds in the heterocrystals is weakened compared to that obtained from the measurement of pure AgNPs. This behavior is due to the shielding effect caused by Fe<sub>3</sub>O<sub>4</sub> [19, 20]. Comparing both samples, the effect is more pronounced for Ag/Fe<sub>3</sub>O<sub>4</sub> PHE than for Ag/Fe<sub>3</sub>O<sub>4</sub> ODE. This difference

can be related to the morphology dissimilarities, as flower-like structures with a larger Ag-Fe<sub>3</sub>O<sub>4</sub> interface can produce a larger shielding effect compared to dimer-like particles. A similar decay of the absorption peak was also observed in Au/Fe<sub>3</sub>O<sub>4</sub> particles [19, 21]. A control sample of 10 nm magnetite particles was also investigated for comparison (synthesis and characterization details are presented in the supplementary information), the respective UV-vis spectra (red line in figure 4(b)) is consistent with subwavelength sized dielectric spheres [22].

In most reports concerning the studies of surface plasmon resonance on metallic/magnetic hybrid nanoparticles, including Au/Fe<sub>3</sub>O<sub>4</sub> and Ag/Fe<sub>3</sub>O<sub>4</sub>, a red-shift of the metal particle SRP is evidenced. According to some authors, this behavior results from the strong coupling of iron oxide, which exhibits higher values of the real part of the refractive index with respect to the organic solvents [23, 24]. Strikingly, the absorption peak of our prepared Ag/Fe<sub>3</sub>O<sub>4</sub> heteroparticles



**Figure 5.** Schematic representation of the two possible pathways for the seeded-growth formation of Ag/Fe<sub>3</sub>O<sub>4</sub> heterocrystals with different morphology. Heterogeneous nucleation of Fe<sub>3</sub>O<sub>4</sub> to form (a) dimer or (b) flower-like structure.

stays at almost the same position as that of AgNPs. This behavior was also observed by Huang *et al* [20] and can indicate a weak interaction between the building blocks. Some authors also suggest that Fe<sub>3</sub>O<sub>4</sub> growth over the Ag seed does not always occur epitaxially, leading to nearly independent surface plasmonic properties of the metallic nanoparticles [19]. Also, some kind of centrifugation sorting during Ag/Fe<sub>3</sub>O<sub>4</sub> washing steps may have privileged AgNPs with a UV-shifted peak position. Moreover, since the modification of the size of the scattering objects are known to affect the intensity and width of the SPR peak, the observed differences could also be related to the minor changes in the Ag seeds size during the second synthesis step.

Measurements of XAFS were carried out in order to examine the Fe-oxidation states of the iron oxide domains in the heterostructures. A control sample of Fe<sub>3</sub>O<sub>4</sub> nanoparticles was also analyzed for comparison. Figures 4(c) and (d) show the profiles of the x-ray absorption near edge spectra (XANES) and extended x-ray absorption fine structure (EXAFS), respectively, determined for the samples Ag/Fe<sub>3</sub>O<sub>4</sub> ODE and Ag/Fe<sub>3</sub>O<sub>4</sub> PHE, as well as for the iron oxide control sample. According to these results, the pre-edge energy position, the pre-peak features and the EXAFS profiles of both heteroparticle systems are compatible with a structure that combines ferric (Fe<sup>2+</sup>) and ferrous (Fe<sup>3+</sup>) ions [14]. Furthermore, by comparing the obtained results from the Ag/Fe<sub>3</sub>O<sub>4</sub> with those one from the Fe<sub>3</sub>O<sub>4</sub> control sample, one can affirm that the environment of Fe-atoms located in the heterostructures are disposed to form an iron oxide with a stoichiometric Fe<sub>3</sub>O<sub>4</sub> phase.

The study and control of the reaction conditions leading to different heterostructures morphologies has been a topic of

intense research in the last few years. In a pioneering work, Yu *et al* proposed that a charge compensation process within the metal nanoparticle (Au in their case) governs and defines the heterostructure conformation [11]. The nucleation of the iron oxide on the Au surface induces a positive charge at the growth interface, immediately compensated by free electrons of the metal. This charge migration produces electron deficient 'restrained facets' and denies multi-nucleation process. However, a change in the medium's electron-donor capacity by using a slightly polar solvent could compensate the charge induced by the polarized growth plane, and thus allow multi-nucleation. Therefore, the modification of the reaction medium from octadecene to phenyl ether can modify the final heterostructure conformation from dimer-like to flower-like nanoparticles. Figure 5 shows a scheme of the possible pathways for the seeded-growth synthesis of Ag/Fe<sub>3</sub>O<sub>4</sub> heterocrystals starting from a mixture of Ag seeds and Fe precursor. This hypothesis was supported by few authors for noble metal (especially Au) heterostructures [11, 12, 20, 25], and also for other metal-metal oxide combinations, such as FePt/MnO [26]. Flower-like nanoparticles were also produced in highly polar solvents like poly-alcohols [10], supporting the hypothesis that the polarity of the synthesis medium influences the morphology of the heterostructure. Nevertheless, additional reports suggest that other reaction conditions like metal seeds—Fe precursor ratio [27] or metal seed crystallinity [20] could also define the heterostructure configuration.

Magnetization features of both Ag/Fe<sub>3</sub>O<sub>4</sub> systems were investigated in order to understand the influence of the nanoparticle morphology on the macroscopic magnetic behavior. Because the magnetic measurements were performed in highly diluted samples, interparticle dipolar interactions are expected



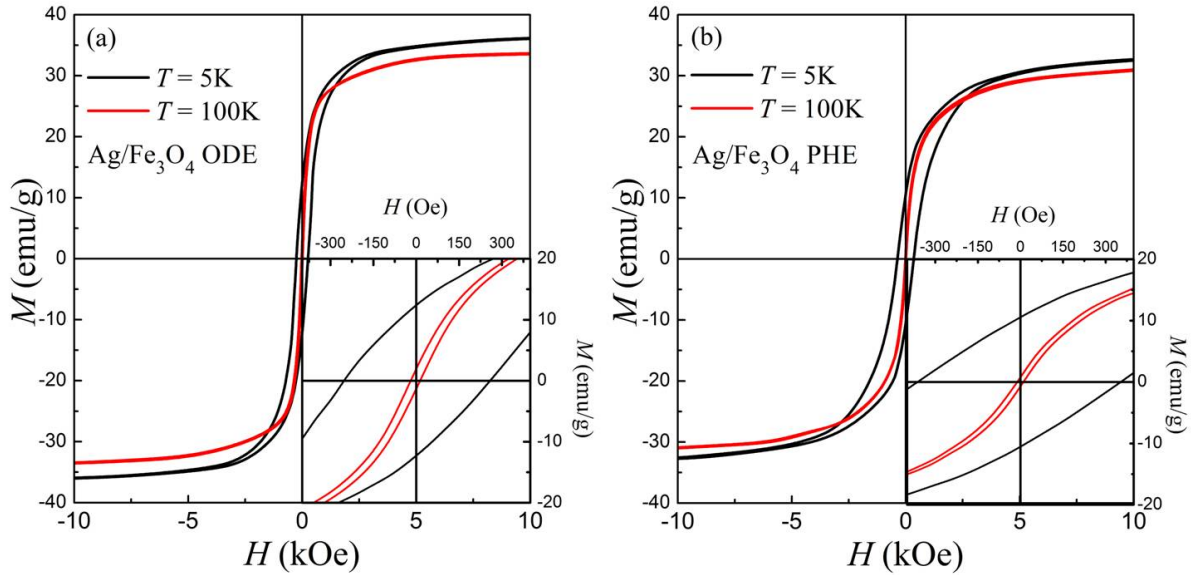


**Figure 6.** Magnetization versus applied magnetic field curves measured at 5 K and 100 K for samples (a) Ag/Fe<sub>3</sub>O<sub>4</sub> ODE and (b) Ag/Fe<sub>3</sub>O<sub>4</sub> PHE. Insets: zoom-in of the low field region showing the coercivity behavior.

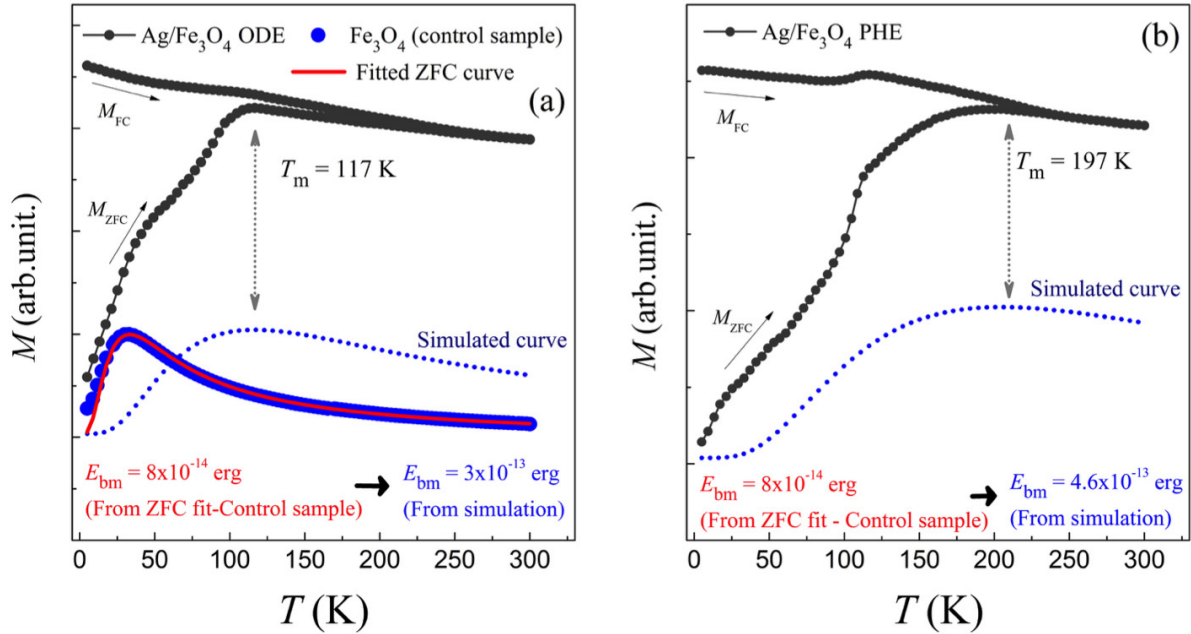


**Figure 7.** ZFC/FC curves taken in a magnetic field of 50 Oe for samples (a) Ag/Fe<sub>3</sub>O<sub>4</sub> ODE and (b) Ag/Fe<sub>3</sub>O<sub>4</sub> PHE. Blue filled symbols in (a) indicate the experimental ZFC curve of the magnetite control sample and the red solid line its respective fit according to equation (1). Blue dotted lines denote the simulated curves for the heterostructures according to equation (1).

to be negligible. However, on the sample with flower-like morphology, the presence of several Fe<sub>3</sub>O<sub>4</sub> domains attached to a single Ag seed can lead to intra particle dipolar and/or exchange interactions, because these magnetic domains can be in direct contact with each other and not spatially separated by the diamagnetic matrix.

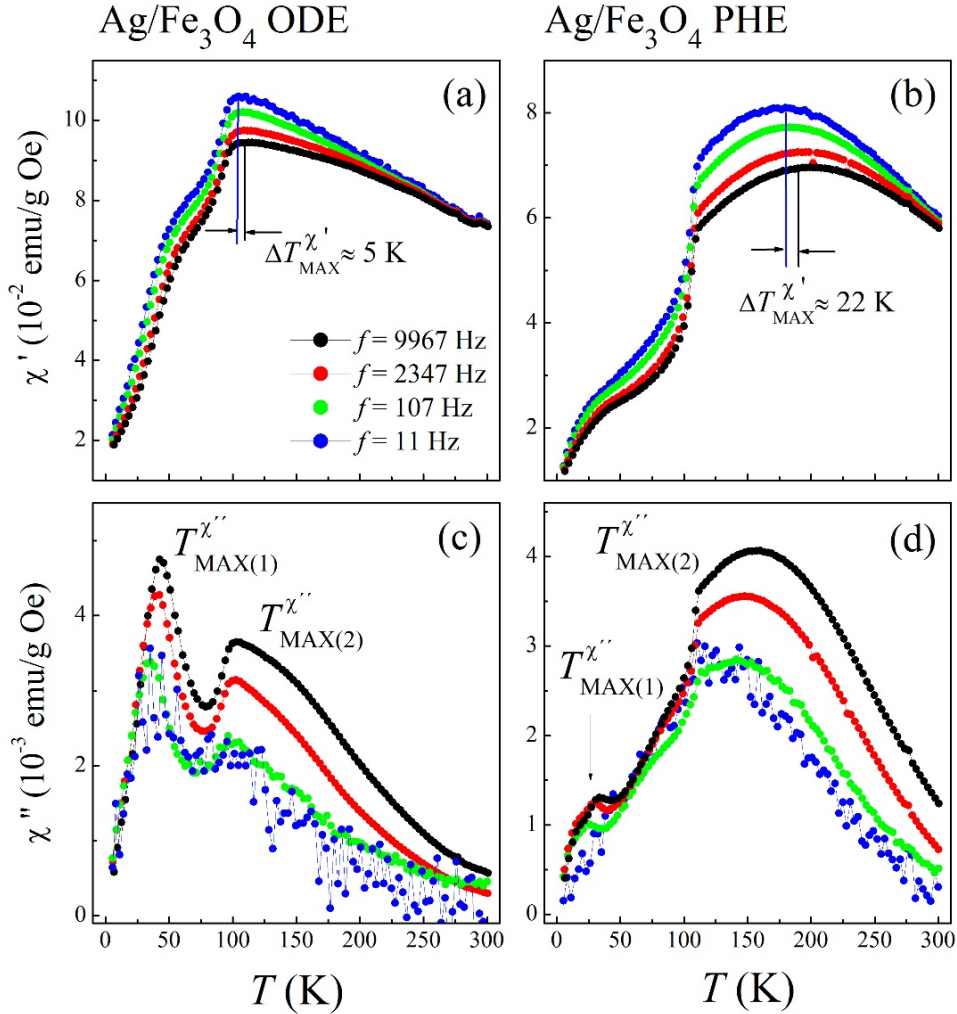
Figure 6 shows the magnetization versus applied field ( $M$  versus  $H$ ) curves performed at 5 K and 100 K. Notice that the magnetization units are expressed in terms of emu per mass of heteroparticles, i.e. mass of Fe<sub>3</sub>O<sub>4</sub> and Ag. While the saturation magnetization ( $M_S$ ) values are lower than those reported for bulk magnetite, as expected for nanoscale magnetic materials,

these are partially underestimated because the additional mass of silver. The S-shaped curves can be related to the presence of monodomain magnetic iron oxide nanoparticles. At  $T = 5$  K the magnetization loops display a coercive field of ~260 Oe for the Ag/Fe<sub>3</sub>O<sub>4</sub> ODE sample and ~360 Oe for the Ag/Fe<sub>3</sub>O<sub>4</sub> PHE sample, indicating that the nanoparticles are at the magnetically blocked regime at this temperature [28]. As can be noted, the coercive field at 5 K is larger in the Ag/Fe<sub>3</sub>O<sub>4</sub> PHE sample than in the Ag/Fe<sub>3</sub>O<sub>4</sub> ODE sample. This behavior can be understood from two main approaches: (i) because the presence of several iron oxide domains attached to the same AgNP in the sample with a flower-like architecture promotes a



**Table 1.** Parameters  $E_{bm}$ ,  $T_{bm}$ ,  $K$  and  $T_i$  obtained from the ZFC fit ( $\text{Fe}_3\text{O}_4$ ) and from simulations ( $\text{Ag}/\text{Fe}_3\text{O}_4$  heterostructures).

Sample	$E_{bm}$ (erg)	$T_{bm}$ (K)	$K$ (erg $\text{cm}^{-3}$ )	$T_i$ (K)
$\text{Fe}_3\text{O}_4$ (control sample)	$8.0 \times 10^{-14a}$	21 <sup>a</sup>	$2.4 \times 10^{5a}$	—
$\text{Ag}/\text{Fe}_3\text{O}_4$ ODE (dimer-like morphology)	$3.0 \times 10^{-13b}$	73 <sup>b</sup>	$9.0 \times 10^{5b}$	170
$\text{Ag}/\text{Fe}_3\text{O}_4$ PHE (flower-like morphology)	$4.6 \times 10^{-13b}$	120 <sup>b</sup>	$1.4 \times 10^{6b}$	200

<sup>a</sup> Values extracted from the fit of the ZFC curve.<sup>b</sup> Simulated values.**Figure 8.** Temperature dependence of the (a) and (b) real  $\chi'(T)$  and (c) and (d) imaginary  $\chi''(T)$  components of the susceptibility of the  $\text{Ag}/\text{Fe}_3\text{O}_4$  heterostructures.

strengthening of dipole–dipole interactions between the magnetic entities [12], which could produce a magnetic hardening in this sample. (ii) Because the effective coupling between the components can alter the arrangement of those magnetic moments located at the magnetic surface and thus modifies the magnetization dynamics. The coercive field in both samples drastically diminishes at 100 K, an indication that the magnetization behavior is close to the superparamagnetic regime [28].

Temperature dependence of the magnetization of  $\text{Ag}/\text{Fe}_3\text{O}_4$  heterostructures, recorded under zero-field-cooling ( $M_{ZFC}$ ) and field-cooling ( $M_{FC}$ ) protocols, is presented in figure 7. In both curves, the ZFC magnetization display a clear and broad maximum value, at  $T_m = 117$  K for  $\text{Ag}/\text{Fe}_3\text{O}_4$  ODE and at  $T_m = 197$  K for  $\text{Ag}/\text{Fe}_3\text{O}_4$  PHE. Although in principle,  $T_m$  can

be associated to the blocked-to-superparamagnetic transition of the iron oxide domains, the obtained values are approximately one magnitude of order larger than ones obtained for the magnetite control sample, which was found at  $T_m = 27$  K (blue symbols in figure 7(a)) and whose shape can be easily linked to a weakly interacting monodomain system [28, 29]. The differences of  $T_m$  between the control sample and the more complex nanostructures can be explained considering three different phenomena: changes in the size of the magnetic nanoparticles [30], strengthening of dipolar interactions [31] and variations in the iron oxide phases [32]. However, for both heterostructures the sizes of the magnetic domains are quite similar; hence the magnetic phase remains unaltered and the dipole–dipole and superexchange interactions should not

strong enough to generate a shift of  $T_m$  of 90 K and 170 K in the Ag/Fe<sub>3</sub>O<sub>4</sub> ODE and Ag/Fe<sub>3</sub>O<sub>4</sub> PHE samples, respectively (in comparison to the control Fe<sub>3</sub>O<sub>4</sub> sample). Such interactions, especially in the sample with flower-like morphology, could affect the effective anisotropy of the structures, leading to a  $T_m$  displacement (as discussed previously) but in a weaker degree. Generally speaking, the  $T_m$  shift (as well as the ZFC/FC general curve shape) can be influenced by the morphology, metal seeds features and/or interface effects. For instance, some authors suggest that the coupling efficiency between metal/Fe-oxide surfaces can modify the superficial disorder [33, 34], the energy barrier ( $E_b$ ) and the magnetocrystalline anisotropy ( $K$ ) of the magnetic counterpart [35], altering the global magnetic behavior of the system. Therefore, two ZFC curves, with values for  $T_m$  matching those obtained from the experimental measurements of the Ag/Fe<sub>3</sub>O<sub>4</sub> heteroparticles were simulated following the expression reported in [36], which is:

$$M_{ZFC}(T) \cong \frac{M_S^2 H}{3K} \left[ \frac{E_{bm}}{k_B} \int_0^{T/T_{bm}} \frac{1}{T} y f(y) dy + \int_{T/T_{bm}}^{\infty} f(y) dy \right], \quad (1)$$

where  $f(y)$  is a distribution of energy barriers (adopted as lognormal-type),  $y = E_b/E_{bm}$  being  $E_b$  and  $E_{bm}$  the energy barrier and the mean energy barrier, respectively.  $T_{bm}$  is the mean blocking temperature,  $M_S$  the saturation magnetization,  $H$  the external magnetic field (50 Oe),  $K$  the anisotropy and  $k_B$  the Boltzmann constant. These simulations allow us to approximately quantify the variations on  $E_{bm}$  and  $K_{ef}$  suggested by the mentioned factors. As expected, the  $E_{bm}$  values extracted from the simulated curves (blue dotted lines in figure 7) are larger in comparison to the one obtained from the ZFC fit of the Fe<sub>3</sub>O<sub>4</sub> control sample:  $\sim 3 \times 10^{-13}$  erg for Ag/Fe<sub>3</sub>O<sub>4</sub> ODE sample,  $\sim 4.6 \times 10^{-13}$  erg for Ag/Fe<sub>3</sub>O<sub>4</sub> PHE sample, and  $\sim 8 \times 10^{-14}$  erg for the Fe<sub>3</sub>O<sub>4</sub> control sample. It is worth noting that the increase in  $E_{bm}$  also raises the anisotropy constant, whose mean value can be obtained from  $K = E_{bm}/V$ , being  $V$  the mean particle volume. Using this expression and assuming a mean diameter of 8.6 nm for the Fe<sub>3</sub>O<sub>4</sub> nanocrystals, the  $K$  values are  $9.0 \times 10^5$  erg cm<sup>-3</sup> and  $1.4 \times 10^6$  erg cm<sup>-3</sup> for dimer and flower-like samples, respectively. These values are approx. 3.5 and approx. 6 times larger than the obtained for the Fe<sub>3</sub>O<sub>4</sub> control sample ( $K$  from fit procedure is  $2.4 \times 10^5$  erg cm<sup>-3</sup>). All the obtained values are summarized in table 1. Larger values of  $E_{bm}$  and  $K$  can be partially attributed to an additional superficial disorder at the Ag/Fe-oxide interface. In that interface, magnetic moments could be isotropically pinned and still coupled with the magnetic moments of the magnetite core, generating a magnetic drag over the core that leads to the increase of the anisotropy [37]. Consequently, the coupling effects will be more significant for the sample with a greater interface between the two components, Ag/Fe<sub>3</sub>O<sub>4</sub> PHE in this case.

Notice that it is not enough to just increase the value of the barrier energy (or  $K$ ) to reproduce exactly the shape and the temperature evolution of the experimental ZFC curves obtained from the dual Ag/Fe<sub>3</sub>O<sub>4</sub> heterostructures. In order to achieve this goal for these complex structures, several other factors need to be considered, such as the dipolar interactions,

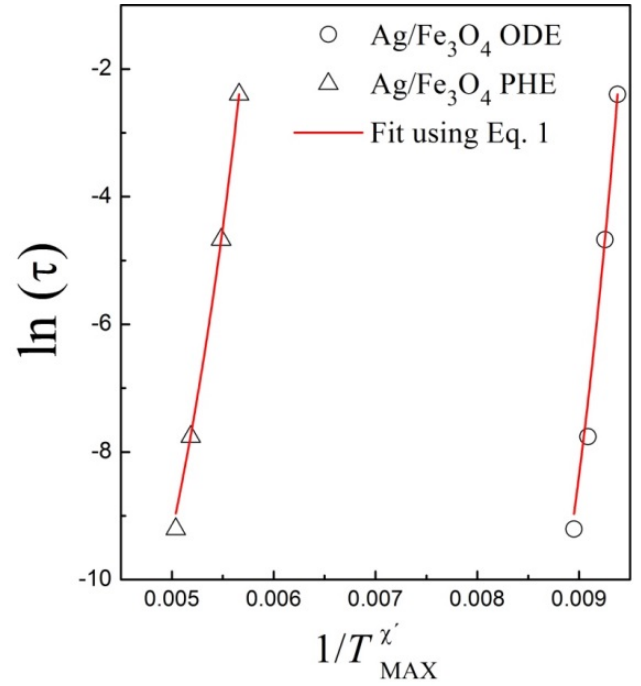


**Figure 9.** Plots of  $\ln(\tau)$  versus  $1/T_{MAX}^{\chi'}$  and the respective fit according to equation (1) (red solid line). Here,  $T_{MAX}^{\chi'}$  is the broader peak of the real component for every measured frequency.

possible effects of spin or charge transfer [38, 39] and cation exchange effects [40], structural defects [41] among others.

Relevant information can also be qualitatively extracted from the FC magnetization curves. For example, the flattened behavior at low temperatures ( $T \leq 50$  K) followed by a wider shoulder as the temperature increases could be a signature of limited nanoparticle aggregation and occurrence of a spin-glass and/or interacting superparamagnetic behavior [29, 42, 43]. Moreover, the manifestation of an irreversibility temperature ( $T_i$ ), defined as the point in which the ZFC curve bifurcates from the FC one, indicates the presence of a distribution of blocking temperatures, as expected for size distributed magnetic monodomains. In summary, all examined properties suggest that the magnetic behavior of the studied samples are a consequence of a sum of several effects, leading to a complex interpretation of the magnetic results.

AC susceptibility measurements were performed to reinforce the results from DC magnetic characterizations. The real and imaginary components of the magnetic susceptibility versus temperature ( $\chi'$  versus  $T$  and  $\chi''$  versus  $T$ ), recorded at four different frequencies, are shown in figure 8. Although the  $\chi'(T)$  curves for Ag/Fe<sub>3</sub>O<sub>4</sub> nanoparticles follow different trends, two main features can be highlighted in both systems: an initial shoulder at low temperatures followed by a broader peak near the  $T_m$  value obtained from the ZFC measurements. The nature of these events can be related with two independent blocked-to-unblocked system processes. The equivalent two events in the imaginary component of the magnetic susceptibility  $\chi''(T)$  is reflected in the presence of two peaks, which are labeled as  $T_{MAX(1)}^{\chi''}$  and  $T_{MAX(2)}^{\chi''}$  in figures 8(c) and (d). The initial shoulder at  $\chi'(T)$  is correlated to the first peak in  $\chi''(T)$

**Table 2.** Extracted and calculated parameters from the AC magnetic susceptibility measurements.

Sample	$T_{\text{MAX}}^{\text{ZFC}}$ (K)	$T_{\text{MAX}}^{\text{'}}$ (K)				$T_{\text{MAX}}^{\text{'}}$ (K)								$E_{\text{b}}$ (erg)	$T_0$ (K)
		$f$ (Hz)				$f$ (Hz)—peak 1				$f$ (Hz)—peak 2					
		11	207	2347	9967	11	207	2347	9967	11	207	2347	9967		
Flower Ag/Fe <sub>3</sub> O <sub>4</sub> ODE	108	104	105	106	107	35	35	41	42	98	100	102	104	$8 \times 10^{-14}$	92
Dimer Ag/Fe <sub>3</sub> O <sub>4</sub> PHE	205	180	183	188	190	23	24	31	34	144	145	149	157	$2 \times 10^{-13}$	133

as expected, and can be assigned to the blocked-to-unblocked transition of those iron oxide nanoparticles non-linked or weakly-linked with the Ag seeds. These temperature values are at similar positions to the ones observed in homogeneously nucleated nanoparticles (control Fe<sub>3</sub>O<sub>4</sub> sample), as shown in figure S5 (supporting information). The second event, evidenced as a peak at  $T \approx 110$  K for the Ag/Fe<sub>3</sub>O<sub>4</sub> ODE sample and  $T \approx 170$  K for the Ag/Fe<sub>3</sub>O<sub>4</sub> PHE sample in the  $\chi'(T)$  and  $\chi''(T)$  curves, is related to the unblocking processes of the Fe<sub>3</sub>O<sub>4</sub> domains attached on the heterostructures or, in the case of flower-like sample with the unblocked-blocked transition of those magnetic nanoparticles with higher inter-particle interaction. Notice that these peaks are registered at higher temperatures for the sample with flower-like morphology, an indication that in this sample the blocking/unblocking process requires more thermal energy to occur. This behavior also supports the previous evidence of the distinct interactions and possible alterations on the magnetocrystalline anisotropy between both systems.

The relative height of the peaks observed in the imaginary component of the magnetic susceptibility has significant differences, i.e. for the Ag/Fe<sub>3</sub>O<sub>4</sub> ODE sample,  $T_{MAX(1)}''$  is higher than  $T_{MAX(2)}''$ , while for the Ag/Fe<sub>3</sub>O<sub>4</sub> PHE sample the opposite occurred. This difference can be related to the ratio of homogeneous to heterogeneous Fe<sub>3</sub>O<sub>4</sub> domains, indicating that the reaction in phenyl ether avoids the homogeneous nucleation events and is more effective to produce heterostructures.

From the AC magnetization results, it is also possible to observe  $T_{MAX}$  displacements as frequency function. Such displacements are rather small when compared to the ones observed in highly interacting nanoparticle systems, a qualitative indication that the magnetic entities can be in a weakly interacting state [29, 31, 44, 45]. To clarify this point, the frequency dependence of the peaks in  $\chi'(T)$  was analyzed for both Ag/Fe<sub>3</sub>O<sub>4</sub> systems by fitting the experimental data using the Vogel–Fulcher law, given by:

$$\tau = \tau_0 \exp(E_b/k_B (T - T_0)) \quad (2)$$

where  $\tau$  is the relaxation time that is associated to the frequency  $f$  through  $\tau = 1/f$ ,  $\tau_0$  is the characteristic time (ranging between  $10^{-9}$  s and  $10^{-12}$  s [46]),  $k_B$  is the Boltzmann constant,  $E_b$  is the energy barrier and  $T_0$  is a characteristic temperature that defines if the thermal energy ( $T > T_0$ ) or the interacting energy ( $T < T_0$ ) dominates the magnetic moment dynamics and magnetization process. By plotting the experimental data as  $\ln(\tau)$  against  $1/T_{MAX}'$  (being  $T_{MAX}'$  the peak associated to the blocking-unblocking processes of heterogeneous nucleated Fe<sub>3</sub>O<sub>4</sub> domains) and using equation (2) to fit them

(figure 9), parameters with coherent physical meaning were obtained. For  $E_b$ , the determined values are  $8 \times 10^{-14}$  erg for Ag/Fe<sub>3</sub>O<sub>4</sub> ODE and  $2 \times 10^{-13}$  erg for Ag/Fe<sub>3</sub>O<sub>4</sub> PHE, which are closer to the ones extracted from the analysis of the ZFC curves. Moreover, the obtained characteristic time  $\tau_0$  ( $\sim 10^{-11}$  and  $\sim 10^{-10}$  s for the Ag/Fe<sub>3</sub>O<sub>4</sub> ODE and Ag/Fe<sub>3</sub>O<sub>4</sub> PHE samples, respectively) matches very well with those obtained from nanoparticle systems with moderate or weak interacting magnetic nanoparticles [46]. The larger values of  $T_0$  determined for the sample with flower-like morphology also indicate a strengthening of the dipole–dipole and exchange forces due to intraparticle interactions. Using the Vogel–Fulcher law to analyze  $\tau_0$ ,  $E_b$  and  $T_0$  of those magnetic particles attached to the Ag seeds supports the previous conclusions obtained from DC magnetic studies, where larger energy barrier values were detected for linked magnetic nanoparticles. A summary of the extracted magnetic parameters is presented in table 2.

## Conclusions

Controlled synthesis protocols were employed to obtain magnetic-plasmonic nanoheterostructures of Ag/Fe<sub>3</sub>O<sub>4</sub> with two distinct morphologies. By controlling the polarity of the reaction medium, the charge compensation can be tuned, leading to particular architecture formations with Ag and iron oxide nanoparticles, resulting in dimer and flower-like configurations. Despite the fact that the magnetite nanoparticles in the heterocrystals have similar sizes and shapes, the magnetization response seems to reflect different phenomena. The observed dissimilarities on the AC and DC magnetization responses can be related to several factors. In the flower-like sample, the dipolar interactions between the Fe-oxide nanoparticles are stronger than in dimer-like counterpart. Also, in flower-like configuration one could have exchange interactions among Fe-atoms of neighboring particles, owing to the existence of percolated regions. Comparing the magnetic parameters of both Ag/Fe<sub>3</sub>O<sub>4</sub> samples with the Fe<sub>3</sub>O<sub>4</sub> control sample and performed simulations, we detected important modifications in the magnetic response. The maximum of the zero-field-cooling curve was shifted around 90 K and 170 K for dimer and flower-like samples, respectively. Furthermore, the inferred magnetic anisotropies also reveal important variations. While part of these changes can be understood in terms of the strengthening of dipolar interactions or variations in the iron oxide phases, we also addressed the observed magnetic complex behavior from the coupling efficiency between metal/Fe-oxide and its role on the superficial disorder and hence on the magnetization response.



## Acknowledgments

O M-L and M K acknowledge FAPESP and CNPq Brazilian agencies (2014/26672-8). The authors from Argentina thank CONICET. Brazilian Synchrotron Light Laboratory (LNLS/CNPEM) is acknowledged for XAS measurements (XAFS-17726). Brazilian Nanotechnology National Laboratory (LNNano/CNPEM) is acknowledged for the use of TEM JEOL JEM 2100 (21789) facilities. O M-L also thanks the Laboratory of Materials of the Autonomous University of Manizales (Colombia). IFW-Dresden and LNNano/CNPEM are acknowledged for TEM images. The authors thank Sebastian Calderon Velasco (INL, International Iberian Nanotechnology Laboratory) for the valuable contributions to the discussion.

## ORCID iDs

O Moscoso Londoño  <https://orcid.org/0000-0003-3366-579X>

## References

- [1] Melinon P, Begin-Colin S, Duvail J L, Gauffre F, Boime N H, Ledoux G, Plain J, Reiss P, Silly F and Warot-Fonrose B 2014 *Phys. Rep.* **543** 163–97
- [2] Xia Y, Gilroy K D, Peng H C and Xia X 2017 *Angew. Chem., Int. Ed. Engl.* **56** 60–95
- [3] Veverka M, Zaveta K, Kaman O, Veverka P, Knizek K, Pollert E, Burian M and Kaspá P 2014 *J. Phys. D: Appl. Phys.* **47** 065503
- [4] Costa L S and Zanchet D 2017 *Catal. Today* **282** 151–8
- [5] Wang C, Yin H, Dai S and Sun S 2010 *Chem. Mater.* **22** 3277–82
- [6] Amarjargal A, Tijing L D, Im I T and Kim C S 2013 *Chem. Eng. J.* **226** 243–54
- [7] Gong P, Li H, He X, Wang K, Hu J, Tan W, Zhang S and Yang X 2007 *Nanotechnology* **18** 285604
- [8] Brollo M E F, Orozco-Henao J M, López-Ruiz R, Muraca D, Dias C S B, Pirota K R and Knobel M 2016 *J. Magn. Magn. Mater.* **397** 20–7
- [9] Das R, Rinaldi-Montes N, Alonso J, Amghouz Z, Garaio E, García J A, Gorria P, Blanco J A, Phan M H and Srikanth H 2016 *ACS Appl. Mater. Interfaces* **8** 25162–69
- [10] Sun L, He J, An S, Zhang J and Ren D 2013 *J. Mol. Struct.* **1046** 74–81
- [11] Yu H, Chen M, Rice P M, Wang S X, White R L and Sun S 2005 *Nano. Lett.* **2** 379–82
- [12] Moscoso-Londoño O, Muraca D, Tancredi P, Cosio-Castañeda C, Pirota K R and Socolovsky L M 2014 *J. Phys. Chem. C* **118** 13168–76
- [13] Sun Y 2015 *Natl Sci. Rev.* **2** 329–48
- [14] Brollo M E, Lopez-Ruiz R, Muraca D, Figueroa S J, Pirota K R and Knobel M 2014 *Sci. Rep.* **4** 6839
- [15] Chandra S, Huls N A, Phan M H, Srinath S, Garcia M A, Lee Y, Wang C, Sun S, Iglesias O and Srikanth H 2014 *Nanotechnology* **25** 055702
- [16] Choi S H et al 2008 *J. Am. Chem. Soc.* **130** 15573–80
- [17] Hyeon T, Lee S S, Park J, Chung Y and Na H B 2001 *J. Am. Chem. Soc.* **123** 12798–801
- [18] Vreeland E C et al 2015 *Chem. Mater.* **27** 6059–66
- [19] Wang C, Xu C, Zeng H and Sun S 2009 *Adv. Mater.* **21** 3045–52
- [20] Huang J, Sun Y, Huang S, Yu K, Zhao Q, Peng F, Yu H, Wang H and Yang J 2011 *J. Mater. Chem.* **21** 17930
- [21] Wei Y, Klajn R, Pinchuk A O and Grzybowski B A 2008 *Small* **4** 1635–9
- [22] Gallo J, García I, Padro D, Arnáiz B and Penadés S 2010 *J. Mater. Chem.* **20** 10010–20
- [23] Hao D, Cheng-Min S, Chao H, Zhi-Chuan X, Chen L, Yuan T, Xue-Zhao S and Hong-Jun G 2010 *Chin. Phys. B* **19** 066102
- [24] Zhang L, Dou Y H and Gu H C 2006 *J. Colloid Interface Sci.* **297** 660–4
- [25] Fantechi E et al 2017 *Chem. Mater.* **29** 4022–35
- [26] Schladt T D, Graf T, Köhler O, Bauer H, Dietzsch M, Mertins J, Branscheid R, Kolb U and Tremel W 2012 *Chem. Mater.* **24** 525–35
- [27] Muraca D, Sharma S K, Socolovsky L M, de Siervo A, Lopes G and Pirota K R 2012 *J. Nanosci. Nanotechnol.* **12** 6961–7
- [28] Knobel M, Nunes W C, Socolovsky L M, Biasi E D, Vargas J M and Denardin J C 2008 *J. Nanosci. Nanotechnol.* **8** 2836–57
- [29] Socolovsky L M and Moscoso-Londoño O 2017 Consequences of magnetic interactions phenomena in granular systems *Complex Magnetic Nanostructures—Synthesis, Assembly and Applications* ed S K Sharma (Berlin: Springer)
- [30] Orozco-Henao J M, Coral D F, Muraca D, Moscoso-Londoño O, Mendoza Zélis P, Fernandez van Raap M B, Sharma S K, Pirota K R and Knobel M 2016 *J. Phys. Chem. C* **120** 12796–809
- [31] Moscoso-Londoño O et al 2017 *J. Magn. Magn. Mater.* **428** 105–18
- [32] Tancredi P, Rivas Rojas P C, Moscoso-Londoño O, Wolff U, Neu V, Damm C, Rellinghaus B, Knobel M and Socolovsky L M 2017 *New J. Chem.* **41** 15033–41
- [33] Jiang J, Gu H, Shao H, Devlin E, Papaefthymiou G C and Ying J Y 2008 *Adv. Mater.* **20** 4403–7
- [34] Umut E, Pineider F, Arosio P, Sangregorio C, Corti M, Tabak F, Lascialfari A and Ghigna P 2012 *J. Magn. Magn. Mater.* **324** 2373–9
- [35] Muraca D, de Siervo A and Pirota K R 2012 *J. Nanopart. Res.* **15** 1375
- [36] Hansen M F and Mørup S 1999 *J. Magn. Magn. Mater.* **203** 214–6
- [37] Rondinone A J, Liu C and Zhang Z J 2001 *J. Phys. Chem. B* **105** 7967–71
- [38] Pineider F, Fernández C D J, Videtta V, Carlino E, Hourani A A, Wilhelm F, Rogalev A, Cozzoli P D, Ghigna P and Sangregorio C 2013 *ACS Nano* **7** 857–66
- [39] Schick I, Gehrig D, Montigny M, Balke B, Panthöfer M, Henkel A, Laquai F and Tremel W 2015 *Chem. Mater.* **27** 4877–84
- [40] Sytnyk M et al 2013 *Nano. Lett.* **13** 586–93
- [41] Laha S S, Regmi R and Lawes G 2013 *J. Phys. D: Appl. Phys.* **46** 325004
- [42] León Félix L, Coaquira J A H, Martínez M A R, Goya G F, Mantilla J, Sousa M H, Valladares L D L S, Barnes C H W and Moraes P C 2017 *Sci. Rep.* **7** 41732
- [43] Morales M B, Phana M H, Pal S, Frey N A and Srikanth H 2009 *J. Appl. Phys.* **105** 07B511
- [44] Masunaga S H, Jardim R F, Fichtner P F P and Rivas J 2009 *Phys. Rev. B* **80** 184428
- [45] Landi G T, Arantes F R, Cornejo D R, Bakuzis A F, Andreu I and Natividad E 2017 *J. Magn. Magn. Mater.* **421** 138–51
- [46] Lee J S, Tan R P, Wu J H and Kim Y K 2011 *Appl. Phys. Lett.* **99** 062506